*electronics*

MDPI

*Article*

# Adaptive Physics-Informed Neural Network for Capacitor Remaining Useful Life Prediction in DC–DC Converters

**Huimin Wang [1,2], Xiaoyan Zhou [1,2], Jun Hu [1,2], Xuefeng Kong [1,2] and Jun Pan [1,2,*]**

[1] Zhejiang Key Laboratory of Reliability Technology for Mechanical & Electrical Product, Zhejiang Sci-Tech University, Hangzhou 310018, China; huimin.wang@zstu.edu.cn (H.W.); 2024210501082@mails.zstu.edu.cn (X.Z.); 2024220503057@mails.zstu.edu.cn (J.H.); kxf2022@zstu.edu.cn (X.K.)

[2] School of Mechanical Engineering, Zhejiang Sci-Tech University, Hangzhou 310018, China

* Correspondence: panjun@zstu.edu.cn

## Abstract

DC–DC converters are widely used in data centers, aerospace systems, electric vehicles, and renewable energy systems, where their reliability directly affects overall system performance. Among their critical components, capacitors are particularly susceptible to degradation and failure, making accurate capacitor health assessment and remaining useful life (RUL) prediction essential for converter-level reliability. However, capacitor degradation exhibits nonlinear and condition-dependent behavior under coupled electrical and environmental stresses, posing significant challenges to accurate RUL prediction. This paper proposes an online capacitor RUL prediction method for DC–DC converters based on an adaptive physics-informed neural network (PINN). First, capacitor equivalent series resistance (ESR) is estimated online from the converter output voltage ripple and used as a capacitor degradation indicator. An adaptive PINN with learnable physical degradation parameters is then developed to address the limited adaptability of conventional models to nonlinear and varying degradation dynamics. Finally, a step-stress temperature–humidity accelerated degradation experiment was conducted on capacitors embedded in an industrial integrated product, and the extracted ESR trajectories were used for model training and RUL prediction. Experimental results showed that the proposed method substantially improved the accuracy of capacitor degradation-trajectory and RUL predictions. Across the three target-domain training-data cutoffs (800, 1000, and 1400 h), the proposed PINN reduced the mean percentage error of degradation trajectory prediction by 44.9% compared with LSTM and by 38.7% compared with the particle filter (PF). For RUL prediction with 800 h of target-domain training data, the proposed method achieved an RMSE of 99.8 h, compared with 116.5 h for LSTM and 149.1 h for PF, corresponding to reductions of 14.3% and 33.1%, respectively. These results demonstrate the effectiveness of the proposed method for online capacitor health prognostics and RUL prediction in DC–DC converters.

**Keywords:** capacitor in DC–DC converters; remaining useful life prediction; equivalent series resistance; online condition monitoring; physics-informed neural network

Check for updates

Academic Editor: Pedro J. Villegas

Received: 2 October 2026
Revised: 4 November 2026
Accepted: 4 November 2026
Published: 6 November 2026

**Copyright:** © 2026 by the authors. Licensee MDPI, Basel, Switzerland. This article is an open access article distributed under the terms and conditions of the Creative Commons Attribution (CC BY) license.

## 1. Introduction

DC–DC converters are critical power conversion devices widely employed in data centers, electric vehicles, aerospace systems, and renewable energy applications [1,2]. The operational reliability and stability of these converters directly affect the safe and continuous operation of the systems in which they are embedded. The primary function of a DC–DC

converter is to convert a direct-current (DC) voltage level into another DC voltage level. As illustrated in Figure 1, a typical DC–DC converter consists of capacitors, inductors, resistors, metal–oxide–semiconductor field-effect transistors (MOSFETs), and diodes.

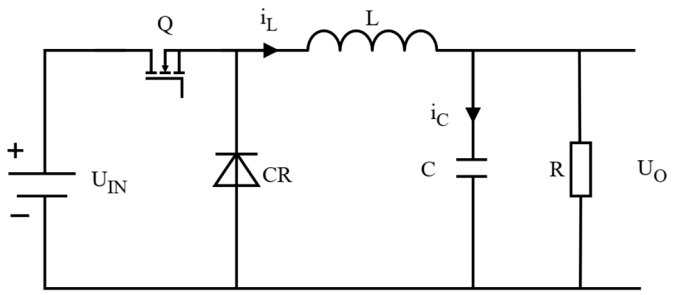



**Figure 1.** Typical structure of a DC–DC converter.

Among these components, capacitors are recognized as one of the most failure-prone devices [3,4]. Consequently, the health condition of capacitors plays a decisive role in determining the reliability and operational stability of DC–DC converters. Accurate modeling of capacitor degradation mechanisms and prediction of their remaining useful life (RUL) are therefore essential for predictive maintenance, reliability enhancement, and lifecycle management of power electronic systems.

Understanding the underlying degradation mechanisms is a prerequisite for accurate prognostics. For aluminum electrolytic capacitors (AECs), degradation is primarily caused by the gradual evaporation of the electrolyte through the sealing structure during long-term operation. The reduction in electrolyte content decreases the effective capacitance while simultaneously increasing the electrolyte resistivity, resulting in a significant rise in equivalent series resistance (ESR) [5]. This degradation process accelerates exponentially with increasing core temperature. In contrast, the degradation of metallized polypropylene film capacitors (MPFCs) is mainly associated with dielectric breakdown and self-healing phenomena [6]. Under high electrical stress, localized micro-arcing events vaporize portions of the metallized electrode layer surrounding defect sites. Although this self-healing mechanism effectively prevents catastrophic short-circuit failures, it permanently reduces the active electrode area and consequently decreases the capacitance. In addition, moisture ingress promotes electrochemical oxidation and increases contact resistance, leading to a gradual increase in ESR [7]. Therefore, capacitor degradation can be generally characterized by a reduction in capacitance and an increase in ESR.

To monitor capacitor degradation, various condition monitoring techniques have been proposed. Existing approaches can generally be classified into model-based observer methods, signal-injection methods, and data-driven methods. In model-based approaches, the inductor voltage has been employed as a fault indicator for DC–DC converters; however, additional auxiliary windings are required for data acquisition [8].

Fourier transform-based methods have also been developed to extract capacitor voltage harmonics without additional hardware [9]. To improve parameter identification efficiency, nonlinear least-squares optimization has been applied to achieve non-intrusive monitoring of converter parameters [10]. Furthermore, adaptive observer-based techniques have been proposed for online estimation of capacitor parameters in buck converters [11]. Considering the frequency-dependent characteristics of capacitors, online ESR tracking algorithms have also been developed and experimentally validated [12].

Signal-injection methods represent another important category of monitoring techniques. For example, multi-level multi-sine excitation signals have been employed to obtain electrochemical impedance information in fuel cells [13]. Low-frequency current ripple

injection methods have also been proposed to assess the degradation severity of aluminum electrolytic capacitors in DC–DC converters [5]. With the rapid advancement of machine learning technologies, data-driven approaches have attracted increasing attention. Support vector machines (SVMs) have been used for soft-fault diagnosis of DC–DC converters based on output voltage fluctuations [14]. In addition, hybrid convolutional neural network (CNN) and long short-term memory (LSTM) architectures have demonstrated excellent feature extraction capability under noisy operating conditions [15].

The acquired degradation indicators can subsequently be used for RUL prediction, which aims not only to assess the current health condition but also to estimate the remaining time before a predefined failure threshold is reached. Existing RUL prediction approaches can generally be divided into physics-based methods and data-driven methods. In physics-based approaches, empirical degradation models are developed according to observed degradation patterns. Considering the nonlinear degradation characteristics of electrolytic capacitors, adaptive two-stage degradation models have been proposed to improve prediction accuracy [16]. Nevertheless, most empirical degradation models assume constant environmental conditions and therefore exhibit limited adaptability under practical operating scenarios characterized by varying temperatures, humidity levels, and loading conditions.

To address these limitations, researchers have investigated data-driven prognostic methods [17]. Deep-learning-based time-series models can capture degradation patterns and identify anomalies [18]. Fuzzy neural networks have been used to predict capacitance and ESR variations [19]. LSTM networks can capture long-term temporal dependencies and have been applied to RUL prediction, including lithium-ion battery prognostics [20]. In power electronics, LSTM-based models have been used for waveform evaluation and data-integrity assessment in photovoltaic applications [21]. Hybrid ARIMA–Bi-LSTM models have also been proposed for capacitor degradation prediction [22]. However, their performance may deteriorate under noisy conditions or when degradation data are limited. CNN-based approaches have been investigated for wind-turbine operational-security prediction, using prediction residuals to assess fault trends and system safety [23]. Adaptive sparse memory networks have also been developed for video object segmentation. These networks improve computational efficiency and robustness by selectively storing and retrieving informative temporal information [24].

Although both physics-based and data-driven approaches possess unique advantages, each exhibits inherent limitations when applied independently [25,26]. Physics-based models often suffer from insufficient adaptability to varying operating conditions, whereas purely data-driven models typically require large amounts of degradation data and may lack physical interpretability.

To overcome these limitations, physics-informed neural networks (PINNs) have recently emerged as a promising framework that integrates physical knowledge with data-driven learning [27,28]. Unlike conventional neural networks, PINNs incorporate governing physical equations directly into the optimization process through additional loss-function constraints, thereby improving model generalization and physical consistency.

The application of PINNs in power electronics has attracted increasing research interest. Recent studies have demonstrated that embedding converter state-space equations into neural network architectures enables highly accurate simulation of closed-loop DC–DC converters under diverse operating conditions [29]. By enforcing Kirchhoff's voltage and current laws through physics-based constraints, PINNs have been shown to outperform conventional fully connected neural networks in transient response modeling. Furthermore, transient-aware PINNs have been proposed for converter parameter estimation without requiring high-frequency measurement circuits [30]. Researchers have also developed dual-

PINN frameworks capable of simultaneously estimating passive component parameters and control variables during transient operation [31].

Despite these advances, existing PINN research in power electronics has primarily focused on short-term dynamic analysis and parameter estimation. Studies addressing long-term degradation evolution and RUL prediction remain extremely limited. In particular, there is a lack of unified frameworks capable of integrating fast electrical dynamics with slow degradation mechanisms over extended operating periods. Consequently, the development of physics-informed prognostic methods for capacitor RUL prediction in DC–DC converters remains an important and largely unexplored research topic.

To address this gap, this paper proposes an online RUL prediction framework for DC–DC converter capacitors by integrating online degradation monitoring with adaptive physics-informed learning. The proposed framework is evaluated using degradation data obtained from step-stress temperature–humidity experiments on an industrial servo controller. The main contributions of this paper are summarized as follows:

1. An adaptive PINN with learnable physical parameters is proposed to address the limited adaptability of conventional models to nonlinear and condition-dependent capacitor degradation, thereby improving degradation trajectory and RUL prediction accuracy.
2. An online ESR estimation method based on two sampled output voltage ripple values within a switching cycle and the inherent circuit parameters of the converter is developed to enable continuous capacitor degradation monitoring during normal operation without interrupting system functionality.
3. A step-stress temperature–humidity accelerated degradation test is conducted on an industrial integrated product to obtain application-oriented degradation data and experimentally evaluate the proposed prognostic framework under varying environmental stress conditions.

The remainder of this paper is organized as follows: Section 2 presents the derivation of the capacitor ESR extraction method based on output voltage ripple analysis. Section 3 introduces the physical degradation model and the proposed adaptive PINN framework. Section 4 describes the accelerated degradation experiments and data acquisition process. Section 5 presents the prediction results and comparative evaluations. Finally, Section 6 concludes the paper and discusses future research directions.

## 2. Capacitor ESR Estimation for DC–DC Converters Operating in Continuous Conduction Mode

The equivalent circuit of the DC–DC converter is illustrated in Figure 2. To facilitate degradation monitoring, the output capacitor is modeled as an ideal capacitor connected in series with an ESR. This simplified model focuses on ESR-related voltage ripple within a switching cycle, while equivalent series inductance (ESL), leakage, and dielectric polarization effects are omitted to reduce model complexity. In Figure 2, Q denotes the power switch, CR represents the freewheeling diode, L is the filter inductor, R denotes the load resistance, $U_{IN}$ is the input voltage, and $U_O$ is the output voltage.

The ESR of a capacitor gradually increases as degradation progresses and can therefore serve as an effective health indicator. To enable online health monitoring without interrupting converter operation, an ESR estimation method based on output voltage ripple analysis is developed in this section.

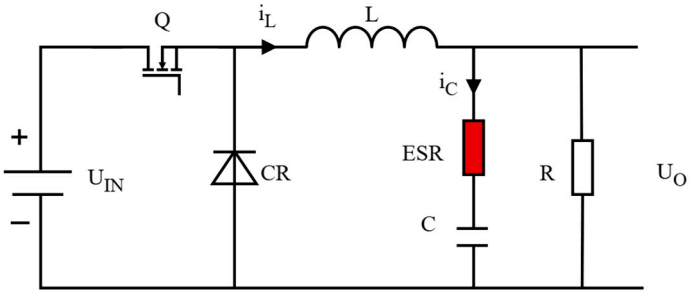



**Figure 2.** Equivalent circuit model of the DC–DC converter with capacitor ESR.

Figure 3 illustrates the key waveforms of the DC–DC converter operating in continuous conduction mode (CCM). The PWM signal controls the switching state of the power switch Q, where $t_{on}$ and $t_{off}$ denote the turn-on and turn-off durations, respectively. The corresponding waveforms include the inductor current $i_L$, capacitor current $i_C$, capacitor voltage $U_C$, ESR voltage $U_{ESR}$, and output voltage $U_O$. $DT$ denotes the instant at which the freewheeling diode transitions from the on-state to the off-state and T denotes the switching period.

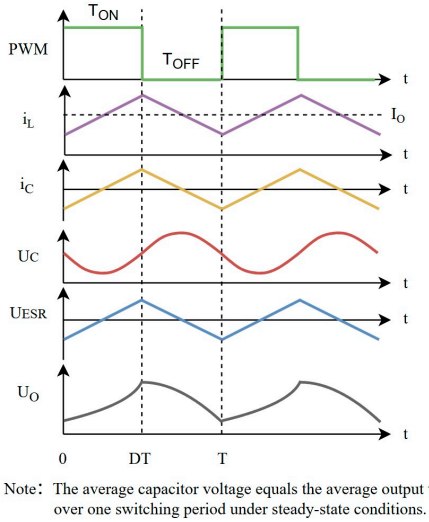



**Figure 3.** Operating waveforms of the DC–DC converter in continuous conduction mode.

By comprehensively analyzing the operating states of the circuit, the relationship between the degradation indicator and the output voltage ripple can be established. When the power switch Q is turned on, the inductor current $i_L$ increases linearly; when the power switch Q is turned off, the inductor current decreases linearly. Throughout one switching period, the inductor current consists of a DC component $I_O$ and a ripple component $\Delta I_L$. When the power switch Q is turned on, the inductor voltage is given by $U_L = U_{IN} - U_O$, and the inductor current increases from $I_O - \Delta I_L/2$ to $I_O + \Delta I_L/2$. According to the voltage–current relationship of the inductor:

$$U_L = L\frac{di_L}{dt} \tag{1}$$

The resulting inductor current variation during this interval is as follows:

$$\triangle I_L = \frac{1}{L}\int_0^{T_{ON}} U_L dt = \frac{(U_{IN} - U_O)T_{ON}}{L} \tag{2}$$

When $DT \leq t < T$, the inductor voltage is $U_L = -U_O$, and the inductor current decreases from $I_O + \Delta I_L/2$ to $I_O - \Delta I_L/2$. Similarly, the inductor current variation during this interval can be expressed as:

$$\triangle I_L = \frac{U_O T_{OFF}}{L} = \frac{U_O(1-D)}{Lf} \tag{3}$$

where $D$ denotes the PWM duty cycle. Combining Equations (2) and (3), the slopes of the inductor current during the rising and falling intervals are $(U_{IN} - U_O)/L$ and $-U_O/L$, respectively. After rearrangement, the inductor current over one switching period can be expressed as the following piecewise function:

$$i_L(t) = \begin{cases} \frac{U_{IN}-U_O}{L}t - \frac{U_O(1-D)}{2Lf} + I_O & (0 \leq t < DT) \\ -\frac{U_O}{L}t + \frac{U_O(1+D)}{2Lf} + I_O & (DT \leq t < T) \end{cases} \tag{4}$$

where $U_{IN}$ is the input voltage, $U_O$ is the average output voltage, $I_O$ is the average output current, $f$ is the switching frequency, and $L$ is the inductance.

Subtracting the average output current from the inductor current yields the capacitor current expression:

$$i_C(t) = \begin{cases} \frac{U_{IN}-U_O}{L}t - \frac{U_O(1-D)}{2Lf} & (0 \leq t < DT) \\ -\frac{U_O}{L}t + \frac{U_O(1+D)}{2Lf} & (DT \leq t < T) \end{cases} \tag{5}$$

Since the capacitor and the ESR are connected in the same branch, the voltage across the ESR can be expressed as follows:

$$ESR \cdot i_C(t) = \begin{cases} ESR[\frac{U_{IN}-U_O}{L}t - \frac{U_O(1-D)}{2Lf}] & (0 \leq t < DT) \\ ESR[-\frac{U_O}{L}t + \frac{U_O(1+D)}{2Lf}] & (DT \leq t < T) \end{cases} \tag{6}$$

The voltage across the capacitor can be expressed as follows:

$$\begin{aligned} U_C(t) &= U_C(0) + \frac{1}{C}\int_0^t i_C(t)dt \\ &= \begin{cases} U_C(0) + \frac{U_{IN}-U_O}{2LC}t^2 - \frac{U_O(1-D)}{2LfC}t & (0 \leq t < DT) \\ U_C(DT) - \frac{U_O}{2LC}t^2 + \frac{U_O(1+D)}{2LfC}t - \frac{U_O D}{2Lf^2C} & (DT \leq t < T) \end{cases} \end{aligned} \tag{7}$$

where $U_C(0)$ denotes the capacitor voltage at t = 0, and $U_C(DT)$ denotes the capacitor voltage at t = $DT$. As shown in the waveform, the capacitor voltage is identical at t = 0, t = $DT$, and t = $T$.

The output voltage can be regarded as the sum of the capacitor voltage and the voltage across the equivalent series resistance (ESR). Therefore, the average output voltage over one switching period is as follows:

$$U_O = \frac{1}{T}\int_0^T U_{ESR}(t) + U_C(t)dt \tag{8}$$

Since the current flowing through the ESR consists solely of an AC component with zero DC component, its integral over one switching period is zero. Therefore, the average output voltage can be expressed as follows:

$$\begin{aligned} U_O = & \frac{1}{T}\int_0^T U_C(t)dt \\ &= \frac{1}{T}\left\{ \begin{array}{l} \int_0^{DT}[U_C(0) + \frac{U_{IN}-U_O}{2LC}t^2 - \frac{U_O(1-D)}{2LfC}t]dt + \\ \int_{DT}^T [U_C(0) - \frac{U_O}{2LC}t^2 + \frac{U_O(1+D)}{2LfC}t - \frac{U_O D}{2Lf^2C}]dt \end{array} \right\} \\ &= U_C(0) + \frac{U_O(D-1)(2D-1)}{12Lf^2C} \end{aligned} \tag{9}$$

Rearranging Equation (9) yields:

$$U_C(0) = U_O[1 - \frac{(D-1)(2D-1)}{12Lf^2C}] \tag{10}$$

By combining Equations (6), (7), and (10) and eliminating $U_C(0)$, the instantaneous output voltage can be expressed as follows:

$$U_O(t) = \begin{cases} ESR[\frac{U_{IN}-U_O}{L}t - \frac{U_O(1-D)}{2Lf}] + U_O[1 - \frac{(D-1)(2D-1)}{12Lf^2C}] \\ +\frac{U_{IN}-U_O}{2LC}t^2 - \frac{U_O(1-D)}{2LfC}t \qquad (0 \le t < DT) \\ ESR[-\frac{U_O}{L}t + \frac{U_O(1+D)}{2Lf}] + U_O[1 - \frac{(D-1)(2D-1)}{12Lf^2C}] \\ -\frac{U_O}{2LC}t^2 + \frac{U_O(1+D)}{2LfC}t - \frac{U_OD}{2Lf^2C} \qquad (\mathrm{DT} \le \mathrm{t} < \mathrm{T}) \end{cases} \tag{11}$$

Subtracting the average output voltage from the instantaneous output voltage yields the expression for the output voltage ripple:

$$\hat{U}_O(t) = \begin{cases} ESR[\frac{U_{IN}-U_O}{L}t - \frac{U_O(1-D)}{2Lf}] - U_O\frac{(D-1)(2D-1)}{12Lf^2C} \\ +\frac{U_{IN}-U_O}{2LC}t^2 - \frac{U_O(1-D)}{2LfC}t \qquad (0 \le t < DT) \\ ESR[-\frac{U_O}{L}t + \frac{U_O(1+D)}{2Lf}] - U_O\frac{(D-1)(2D-1)}{12Lf^2C} \\ -\frac{U_O}{2LC}t^2 + \frac{U_O(1+D)}{2LfC}t - \frac{U_OD}{2Lf^2C} \qquad (\mathrm{DT} \le \mathrm{t} < \mathrm{T}) \end{cases} \tag{12}$$

The above equation quantifies the relationship between the output voltage ripple, the capacitance $C$, and the ESR. To determine the ESR, the voltage ripple at two time instants, t = 0 and t = $DT$, is selected for analysis. By solving the resulting system of equations, the ripple values at these two instants are obtained as follows:

$$\hat{U}_O(0) = -ESR\frac{U_O(1-D)}{2Lf} - U_O\frac{(D-1)(2D-1)}{12Lf^2C} \tag{13}$$

$$\hat{U}_O(DT) = ESR\frac{U_O(1-D)}{2Lf} - U_O\frac{(D-1)(2D-1)}{12Lf^2C} \tag{14}$$

Combining the above two equations and eliminating the capacitance C yields:

$$\hat{U}_O(0) - \hat{U}_O(DT) = -ESR\frac{U_O(1-D)}{Lf} \tag{15}$$

After simplification, the expression can be written as follows:

$$ESR = \frac{Lf[\hat{U}_O(DT) - \hat{U}_O(0)]}{U_O(1-D)} \tag{16}$$

where $\hat{U}_O(DT)$ and $\hat{U}_O(0)$ denote the output voltage ripple values measured at the selected sampling instants, L is the filter inductance, and $f$ represents the switching frequency.

All parameters in the resulting expression, except the two sampled ripple voltages, are known circuit parameters or can be measured. Therefore, ESR can be estimated online using only two output voltage samples acquired during normal converter operation. This approach requires no additional excitation signals, auxiliary sensing circuits, or converter shutdown. It is therefore suitable for condition monitoring and prognostics in practical power-electronic systems.

## 3. Adaptive Physics-Informed Neural Network for Remaining Useful Life Prediction

Figure 4 illustrates the overall framework of the proposed PINN-based prognostic methodology for DC–DC converter capacitors. The framework consists of three major stages:

degradation indicator extraction, model training, and RUL prediction. First, the capacitor ESR is extracted online from the output voltage ripple and used as the health indicator. Subsequently, a PINN incorporating capacitor degradation mechanisms is trained using the extracted degradation trajectories. Finally, the trained model is employed to predict future degradation evolution and estimate the RUL of the capacitor.

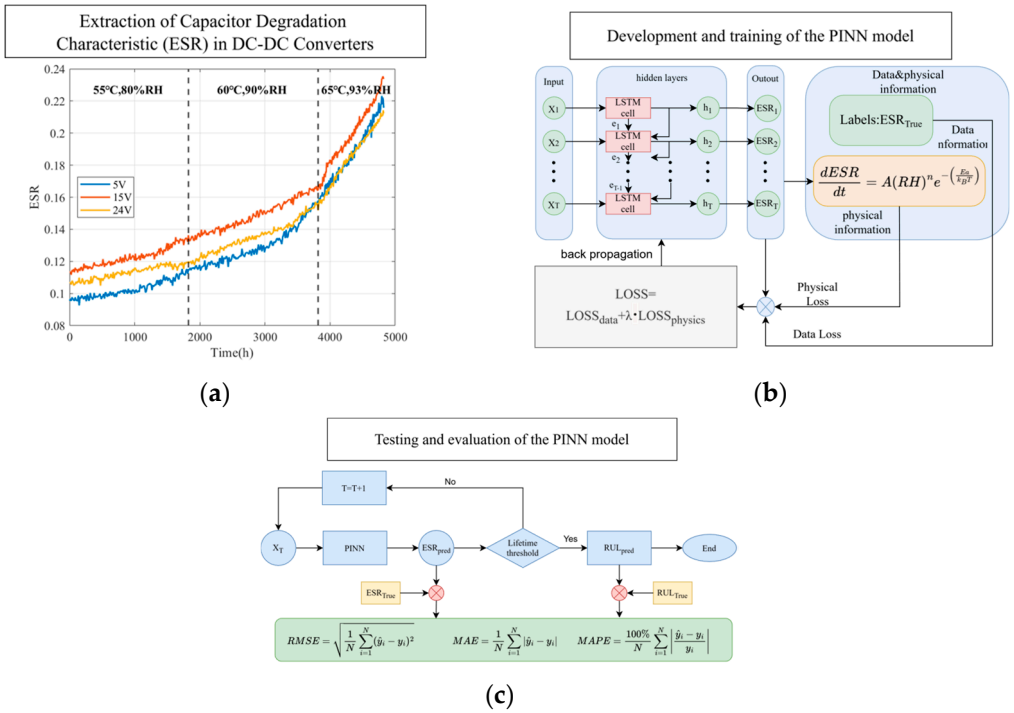



**Figure 4.** Overall framework of the proposed adaptive PINN-based RUL prediction method. (**a**) Extraction of the capacitor degradation indicator. (**b**) Model construction and training. (**c**) Testing and evaluation.

### *3.1. Physics-Based Degradation Model*

For capacitors operating under long-term charge–discharge cycles, ESR is widely recognized as one of the most reliable indicators of health degradation. The increase in ESR reflects the cumulative effects of electrolyte evaporation, electrode corrosion, and dielectric aging. Since these degradation mechanisms are strongly influenced by environmental conditions, both temperature and humidity must be considered in degradation modeling.

To characterize the degradation process, a temperature–humidity-dependent degradation model is adopted based on Peck's empirical acceleration model [32]. This model accounts for the effects of temperature and relative humidity through an Arrhenius-type term and a power-law humidity term. The degradation rate is expressed as follows:

$$\lambda = A \cdot RH^{n} \cdot \exp\left(-\frac{E_a}{kT}\right) \tag{17}$$

where $A$ is a material-dependent constant, $RH$ denotes the relative humidity, $n$ is the humidity acceleration coefficient, $E_a$ represents the activation energy, $k$ is Boltzmann's constant, and T is the absolute temperature.

Conventional reliability models generally assume that $E_a$ and n remain constant throughout the degradation process. However, manufacturing variations, material inconsistencies, and operating-condition uncertainties often cause significant deviations among individual capacitors. Consequently, fixed physical parameters may limit the adaptability and prediction accuracy of traditional degradation models.

To address this issue, the proposed framework treats the activation energy $E_a$ and humidity coefficient $n$ as learnable parameters rather than predefined constants. These parameters are optimized jointly with the neural network weights during training. As a result, the model is capable of automatically identifying the physical characteristics of individual capacitors and adapting to different degradation patterns.

### *3.2. Physics-Informed Neural Network Architecture*

Although deep neural networks possess strong nonlinear approximation capabilities, their performance typically depends on the availability of large quantities of training data. In practical accelerated degradation experiments, however, only limited degradation trajectories can be obtained because of the high cost and long duration of testing. Under such circumstances, purely data-driven approaches are susceptible to overfitting and often lack physical interpretability.

To overcome these limitations, an adaptive PINN framework is developed by integrating physical degradation knowledge into an LSTM-based neural network architecture. The proposed framework combines the feature-extraction capability of deep learning with the physical consistency provided by degradation models.

Capacitor aging is a nonlinear cumulative process with strong temporal dependencies. Therefore, an LSTM network is adopted as the backbone architecture because of its superior ability to capture long-term sequential relationships. Compared with conventional recurrent neural networks (RNNs), LSTM networks effectively alleviate the vanishing-gradient problem through dedicated memory cells and gating mechanisms.

The structure of the LSTM block is illustrated in Figure 5. At each time step t, the network receives a multivariate input vector

$$x_t = [ESR_{t-1}, T_t, RH_t] \tag{18}$$

where $ESR_{t-1}$ denotes the health state at the previous time step, while $T_t$ and $RH_t$ represent the temperature and relative humidity at the current time step, respectively.

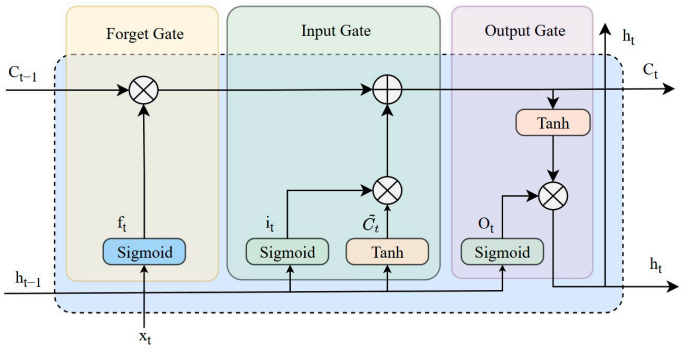



**Figure 5.** Architecture of the LSTM unit employed in the proposed PINN.

After entering the LSTM layer, the input sequence is processed through the forget gate, input gate, and output gate. The forget gate determines which historical degradation information should be retained, whereas the input gate controls the incorporation of newly acquired degradation features. The memory-cell state is then updated by combining historical and current information. Finally, the output gate generates the hidden-state representation used for degradation prediction.

The governing equations of the LSTM unit can be expressed as

$$\begin{aligned} f_t &= \sigma(W_f x_t + U_f h_{t-1} + b_f) \\ i_t &= \sigma(W_i x_t + U_i h_{t-1} + b_i) \\ o_t &= \sigma(W_o x_t + U_o h_{t-1} + b_o) \\ c_t &= f_t \odot c_{t-1} + i_t \odot \tilde{c}_t \\ h_t &= o_t \odot \tanh(c_t) \end{aligned} \tag{19}$$

where $f_t$, $i_t$, and $o_t$ denote the forget, input, and output gates, respectively; $c_t$ is the cell state, $\tilde{c}_t$ is the candidate cell state, and $h_t$ is the hidden state. $W_g$ and $U_g$ represent the input-to-hidden and hidden-to-hidden weight matrices, respectively, and $b_g$ denotes the bias vector, where g ∈ {f, i, o}. The function $\sigma$ is the sigmoid function, tanh is the hyperbolic tangent function, and $\odot$ denotes element-wise multiplication.

By leveraging its memory mechanism, the LSTM network can effectively capture long-term degradation dependencies and establish the nonlinear mapping between environmental stresses and capacitor degradation states.

### *3.3. Physics-Guided Multi-Objective Optimization*

In conventional deep-learning models, network parameters are optimized solely according to prediction errors. Although this strategy often yields excellent fitting performance, it may generate physically inconsistent predictions when extrapolating beyond the available training data.

To improve prediction reliability, physical degradation knowledge is incorporated into the optimization process through a physics-guided loss function. The overall loss function is formulated as

$$L = L_{data} + \alpha L_{physics} \tag{20}$$

where $L_{data}$ denotes the data loss, $L_{physics}$ represents the physics loss, and $\alpha$ is an adaptive weighting coefficient.

The data loss is defined using the mean squared error (MSE) between the predicted ESR trajectory and the measured degradation data:

$$L_{data} = \frac{1}{N}\sum_{t=1}^{N}(y_t - \hat{y}_t)^2 \tag{21}$$

where $y_t$ and $\hat{y}_t$ denote the measured and predicted ESR values, respectively.

To enforce consistency with the physical degradation model, a physics residual is introduced. First, the degradation rate predicted by the neural network is estimated through finite-difference approximation:

$$\dot{y}_t \approx \frac{\hat{y}_{t+1} - \hat{y}_t}{\Delta t} \tag{22}$$

where $\dot{y}_t$ denotes the predicted ESR degradation rate at time t, $\hat{y}_t$ and $\hat{y}_{t+1}$ represent the predicted ESR values at two consecutive time steps, and $\Delta t$ is the time interval between adjacent samples. The theoretical degradation rate is then calculated according to the temperature–humidity acceleration model. The physics loss is defined as the mean squared discrepancy between the predicted degradation rate and the theoretical degradation rate:

$$L_{physics} = \frac{1}{N}\sum_{t=1}^{N}(\dot{y}_t - \lambda_t)^2 \tag{23}$$

In Equation (23), $L_{physics}$ denotes the physics loss, $N$ is the number of samples used to calculate the loss, and $\lambda_t$ represents the theoretical degradation rate at time t, calculated using the temperature–humidity degradation model in Equation (17). Minimizing this loss encourages the neural network to produce degradation trajectories that are not

only consistent with the observed data but also compliant with the underlying physical degradation mechanisms.

During backpropagation, both the neural network parameters and the physical parameters are updated simultaneously. Let $\theta$ denote the network parameters and $\phi = [E_a, n]$ denote the learnable physical parameters. The optimization process can be expressed as

$$\begin{aligned} \theta &\leftarrow \theta - \eta_\theta \nabla_\theta L \\ \phi &\leftarrow \phi - \eta_\phi \nabla_\phi L \end{aligned} \tag{24}$$

where $\eta_\theta$ and $\eta_\phi$ are the learning rates associated with the neural-network parameters and physical parameters, respectively.

To further improve training stability, an adaptive weighting strategy based on the exponential moving average (EMA) is adopted. Because the magnitudes of the data loss and physics loss may differ substantially during training, fixed weighting coefficients can lead to gradient imbalance and suboptimal convergence.

At each training epoch $k$, the target weighting coefficient is calculated as the ratio of the data loss to the physics loss:

$$\alpha_{target}^{k} = \frac{L_{data}^{k}}{L_{physics}^{k}} \tag{25}$$

$$\alpha_{k+1} = \beta \alpha_k + (1 - \beta)\alpha_{target} \tag{26}$$

Equation (25) aims to balance the contributions of the two loss terms by making their weighted magnitudes comparable. The target coefficient is then smoothed using the EMA in Equation (26), where $\beta$ controls the smoothing effect. A larger $\beta$ results in a smoother update, whereas a smaller value allows faster adaptation to changes in the loss magnitudes. In this study, the EMA smoothing coefficient was set to 0.9, and the initial weighting coefficient was set to 0.5. The coefficient was updated once per training epoch during model optimization.

## 4. Step-Stress Accelerated Degradation Experiment of DC–DC Converter Capacitors

To validate the proposed RUL prediction framework, accelerated degradation experiments were conducted on capacitors embedded within practical DC–DC converter systems. Since the ESR of a capacitor gradually increases as aging progresses, ESR was selected as the health indicator throughout the experimental study.

Unlike laboratory-based component testing, this study focused on degradation monitoring under practical application conditions. Therefore, a DC–DC converter integrated into an electro-hydraulic vibration servo controller was selected as the experimental platform.

Figure 6 presents the physical appearance and internal structure of the electro-hydraulic vibration servo controller. The controller incorporates multiple DC–DC converters that provide different voltage levels for various functional modules. During operation, the health condition of the output capacitors directly affects power quality and system reliability.

Figure 7 shows the experimental setup. The experimental setup consisted of an environmental chamber (GWS Test Instrument Co., Ltd., Suzhou, China), a data-acquisition system (Hangzhou ECON Technology Co., Ltd., Hangzhou, China), an oscilloscope (Tektronix, Inc., Beaverton, OR, USA), and a host computer (Lenovo Group Limited, Beijing, China).The chamber maintained the specified temperature and humidity conditions, while the oscilloscope recorded the output voltage ripple of the converters. The host computer managed data collection, storage, and subsequent analysis.

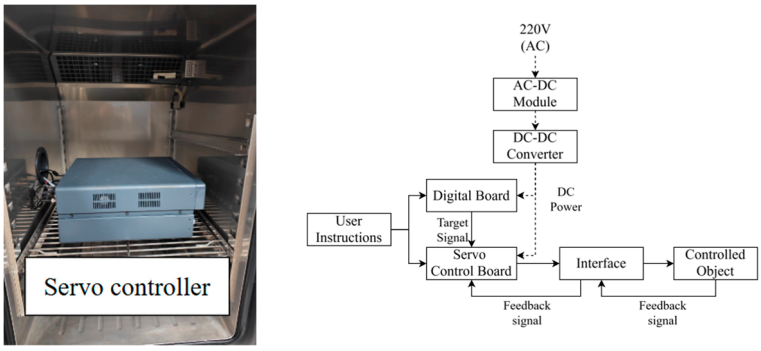



**Figure 6.** Electro-hydraulic vibration servo controller used for accelerated degradation testing.

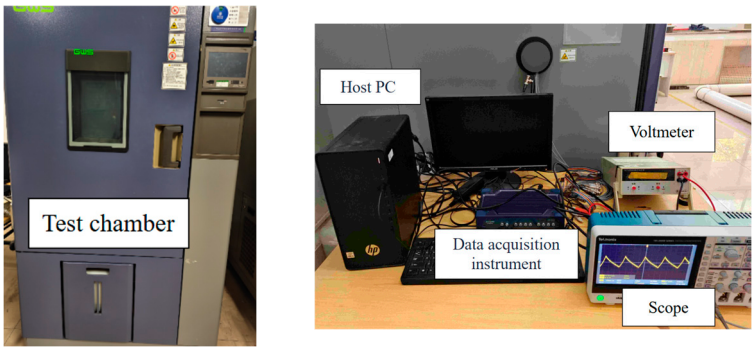



**Figure 7.** Experimental setup for step-stress temperature–humidity accelerated degradation testing.

According to the product specifications, the servo controller contains three representative DC–DC converter channels with nominal output voltages of 5, 15, and 24 V, whose corresponding filter inductances (L) are 100, 150, and 220 μH, respectively, while their output capacitances (C) are 220, 220, and 100 μF, respectively, as summarized in Table 1.

**Table 1.** Electrical Specifications of the Investigated DC–DC Converters.

| Converter No. | Input Voltage (V) | Output Voltage (V) |
|---|---|---|
| 1 | 24 | 5 |
| 2 | 24 | 15 |
| 3 | 36 | 24 |

To accelerate the degradation process while maintaining realistic failure mechanisms, a step-stress temperature–humidity testing strategy was adopted. Compared with constant-stress testing, step-stress acceleration can significantly reduce the experimental duration and better emulate practical operating environments characterized by varying environmental conditions.

The accelerated degradation experiment consisted of three consecutive stress stages:

- Stage I (0–1824 h): Temperature = 55 °C, Relative Humidity = 80% RH;
- Stage II (1824–3816 h): Temperature = 60 °C, Relative Humidity = 90% RH;
- Stage III (>3816 h): Temperature = 65 °C, Relative Humidity = 93% RH.

Throughout the experiment, the servo controller operated continuously in self-closed-loop mode. The same load resistance was applied to all three DC–DC converter channels. Output voltage Ripple was measured periodically using a digital oscilloscope.ESR was then estimated using the analytical model derived in Section 2, and the resulting degradation trajectories were used for model development and evaluation.

Figure 8 presents the ESR degradation trajectories of the three monitored capacitors. Specifically, ESR1 corresponds to the capacitor in the 5 V converter channel, ESR2 corresponds to the capacitor in the 15 V converter channel, and ESR3 corresponds to the capacitor in the 24 V converter channel. The dashed lines indicate the time instants at which the stress conditions are switched.

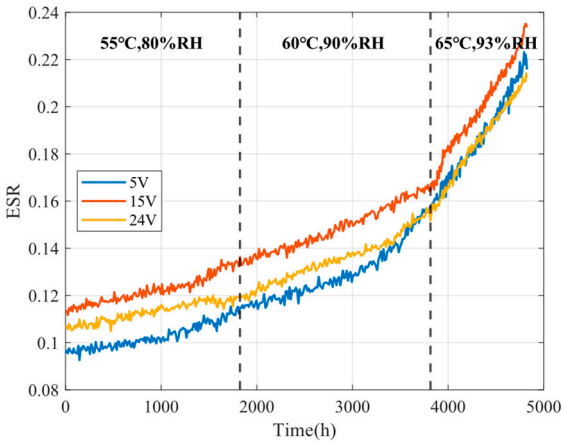



**Figure 8.** ESR degradation trajectories of capacitors under accelerated aging conditions.

As shown in Figure 8, all three capacitor channels exhibited nonlinear ESR growth over time, with more pronounced degradation following the stress transitions. The 15 V channel generally exhibited higher ESR than the other two channels. Small high-frequency fluctuations were superimposed on this overall trend. These fluctuations were primarily attributed to periodic variations in the temperature and humidity regulation system of the environmental chamber, measurement noise associated with the data-acquisition instruments, and sampling uncertainties. Nevertheless, the fluctuations remained relatively small compared with the overall degradation trend and therefore did not affect the extraction of long-term degradation characteristics.

From a physical perspective, elevated temperature accelerates electrolyte evaporation and increases the internal vapor pressure of the capacitor, thereby promoting electrolyte loss through the sealing structure. Simultaneously, high humidity facilitates moisture penetration and accelerates electrochemical corrosion of the internal electrode materials. The combined effect of these mechanisms leads to a reduction in ionic conductivity and an increase in internal resistance. Consequently, the ESR exhibits a nonlinear growth trend that becomes increasingly pronounced during the middle and late stages of degradation.

Furthermore, a noticeable increase in the degradation rate was observed after each stress transition. This finding confirmed the strong dependence of capacitor aging on environmental conditions and highlighted the need to incorporate temperature–humidity effects into the degradation model. The observed degradation trajectories therefore provided an experimental basis for evaluating the proposed physics-informed prognostic framework.

The collected ESR datasets were then used for degradation-trajectory prediction and RUL estimation, as described in the following section.

## 5. Results and Discussion

To evaluate the effectiveness of the proposed adaptive PINN, two representative benchmark methods were selected for comparison. The first benchmark was a conventional long short-term memory (LSTM) network that relied solely on data-driven learning without incorporating physical knowledge. The second was a particle filter (PF)-based approach

that used the same physical degradation model as the proposed method but did not employ neural-network-based feature extraction.

All experiments were conducted using MATLAB R2023a on a Windows 11 platform equipped with an NVIDIA RTX 4050 GPU. The primary hyperparameters of the proposed PINN are summarized in Table 2.

**Table 2.** Parameters of the Proposed PINN Model.

| Parameter | Value |
|---|---|
| Number of LSTM layers | 1 |
| Hidden neurons | 64 |
| Maximum epochs | 250 |
| Initial learning rate | 0.005 |
| Optimizer | Adam |
| Learning rate decay factor | 0.1 |
| Activation functions | Tanh and Sigmoid |

Considering the practical difficulty of obtaining complete lifetime degradation data in industrial applications, a transfer-learning strategy was adopted. Source-domain degradation trajectories from converter channels with different electrical loading conditions were used for pre-training, followed by fine-tuning with the available early-stage observations from the target capacitor. To prevent future-data leakage, the source- and target-domain data used in each forecasting scenario were restricted to observations available at the corresponding forecast origin. The preprocessing parameters were estimated using only the permitted training data and then kept fixed during forecasting. The final test data were excluded from preprocessing, hyperparameter selection, and model training.

To evaluate the proposed method under different levels of target-domain data availability, three fixed-origin forecasting scenarios were considered, with forecast origins at 800, 1000, and 1400 h. For each scenario, the observed target-domain ESR trajectory up to the forecast origin was used for model adaptation, while subsequent observations were reserved exclusively for testing. At each forecast origin, the LSTM hidden and cell states were initialized to zero at the beginning of the available input sequence and propagated chronologically through the observed history. During recursive forecasting, the predicted ESR at each future step was used as the ESR input for the next step. Future temperature and relative-humidity inputs were specified according to the environmental stress schedule available at the forecast origin. The trained network parameters and learned physical parameters remained fixed throughout each forecasting rollout, although the recurrent hidden and cell states were updated as each new prediction was generated. No measured ESR values from the forecast period were used to update the model.

These experiments represented fixed-origin forecasting rather than continuous online model updating. The LSTM and PF baselines were evaluated using the same forecast origins, target-domain observation windows, forecast horizons, and available environmental information to ensure comparable information conditions across methods.

### *5.1. Training Characteristics of the Proposed PINN*

Figure 9a illustrates the evolution of the loss function, while Figure 9b,c show the evolution of the learnable physical parameters. The training loss decreased rapidly during source-domain pre-training and stabilized after target-domain fine-tuning began at epoch 200. Meanwhile, the learned activation energy and humidity exponent converged toward relatively stable values, although their final values differed slightly across the three training-data cutoffs. This difference could be attributed to variations in the observed degradation trajectories and environmental stress conditions. Specifically, the 800 h and 1000 h training

datasets covered different portions of Stage I, whereas the 1400 h dataset also included the initial part of Stage II, during which both temperature and relative humidity increased. Since Ea and n jointly characterize the temperature–humidity dependence of the degradation rate, their estimates could vary with the available training data. Therefore, the converged values should be interpreted as data-dependent parameter estimates rather than evidence of changes in the intrinsic physical properties of the capacitors.

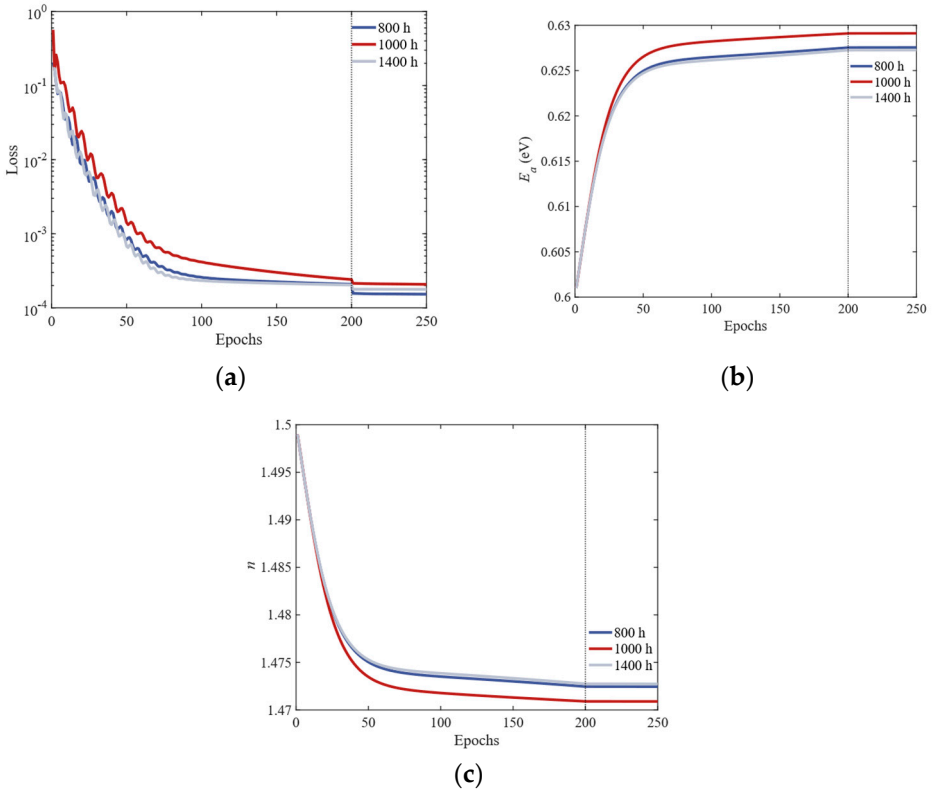



**Figure 9.** Training evolution of the proposed PINN: (**a**) loss convergence, (**b**) activation energy parameter, and (**c**) humidity coefficient parameter.

### *5.2. Degradation Trajectory Prediction Performance*

Figure 10 compares the degradation trajectory prediction results of the three methods under different training-data lengths.

The red line in Figure 10 represents the failure threshold, which is derived from the relevant product specifications [33], while the pink line indicates the starting point of the degradation trajectory prediction.Across all training scenarios, the proposed PINN consistently provided the closest agreement with the measured degradation trajectories. In contrast, the purely data-driven LSTM exhibited increasing prediction deviations during the later stages of degradation, particularly when only limited early-life data are available. This behavior was primarily attributed to insufficient physical constraints during long-term extrapolation.

The PF algorithm demonstrated better physical consistency than the LSTM; however, its prediction accuracy remained limited because it relied exclusively on predefined degradation equations. Consequently, it lacked the flexibility required to capture individual degradation variations and nonlinear characteristics present in real-world degradation data.

By integrating physical degradation knowledge with deep learning, the proposed PINN effectively combined the strengths of both approaches. The network extracted nonlinear temporal features from degradation data while simultaneously enforcing compliance with

the underlying degradation mechanisms. As a result, the predicted degradation trajectories remained accurate throughout the entire prediction horizon.

The corresponding prediction errors are presented in Figure 11. The errors of the LSTM and PF models increased progressively as the prediction horizon extended. In contrast, the proposed PINN maintained relatively small prediction errors even during the late stages of degradation. This behavior indicated better long-term extrapolation capability and improved robustness under limited-data conditions.

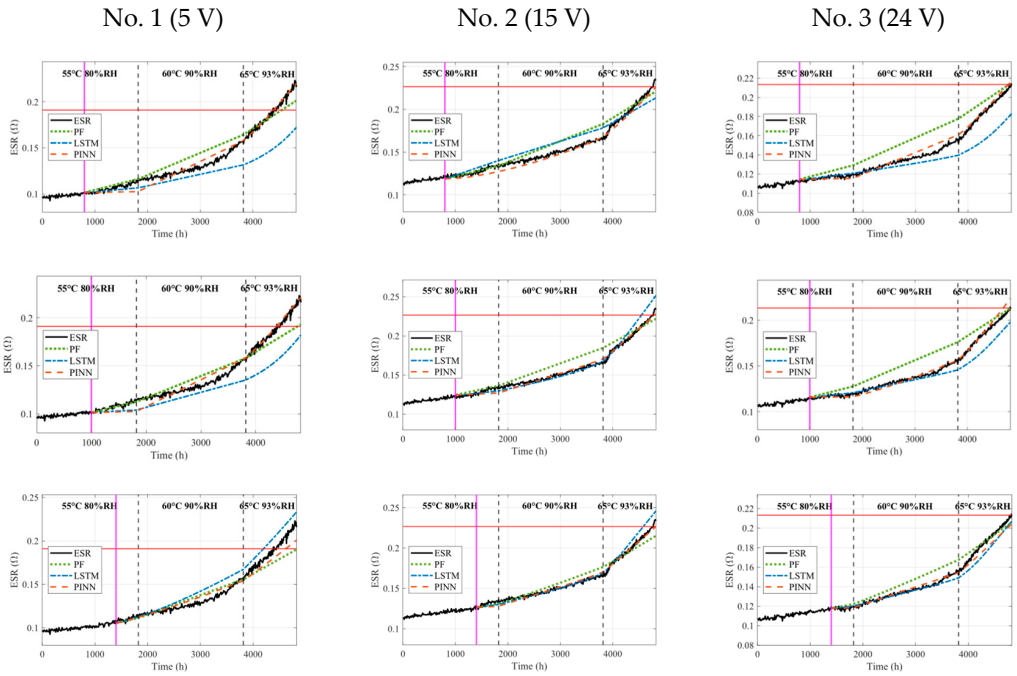



**Figure 10.** Comparison of degradation trajectory prediction results obtained using different methods.

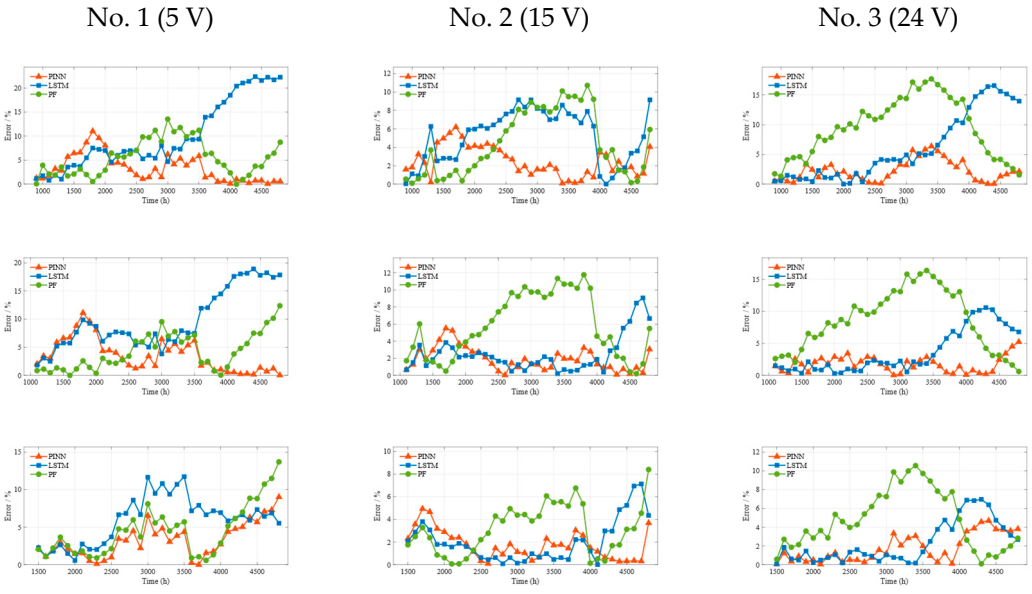



**Figure 11.** Prediction errors of degradation trajectories under different training-data lengths.

To further quantify prediction performance, Figure 12 presents the distributions of degradation trajectory prediction errors under different training-data lengths (800, 1000 and 1400 h).



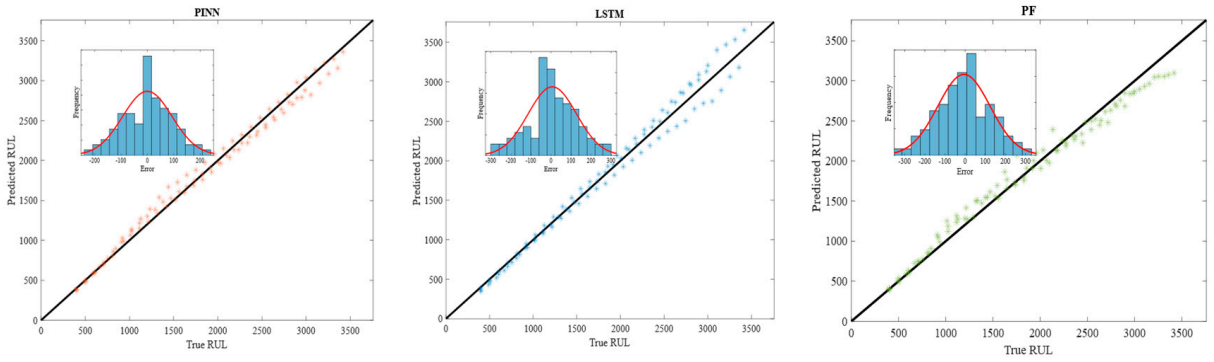

**Figure 12.** Distribution of degradation trajectory prediction errors for different methods.

The results showed that the prediction errors of the proposed PINN were tightly concentrated within a narrow range, whereas the error distributions of the LSTM and PF models were significantly broader. This observation demonstrated that the proposed method improved both prediction accuracy and stability.

Quantitatively, the proposed PINN reduced the mean percentage error by 44.9% compared with the conventional LSTM model and by 38.7% compared with the PF approach. These improvements confirmed the effectiveness of incorporating physical constraints into the learning process, particularly when only limited degradation data were available.

### *5.3. Remaining Useful Life Prediction Performance*

The RUL of each capacitor was estimated by iteratively propagating the predicted degradation trajectory until the predefined failure threshold was reached. Figure 13 presents the RUL prediction results obtained using the first 1400 h of degradation data for training. The proposed PINN produced RUL estimates that closely matched the actual failure times. In comparison, both the LSTM and PF models exhibited larger deviations from the ground truth.




(**a**) (**b**) (**c**)

**Figure 13.** Comparison of RUL prediction results: (**a**) PINN, (**b**)LSTM, and (**c**) PF.

To clarify the RUL calculation in Figure 13, a fixed forecast origin of 1400 h was adopted. For each capacitor channel, the trained model recursively generated a complete future ESR degradation trajectory using the observations available up to the forecast origin. The predicted failure time, $\hat{T}_f$ was determined as the first time at which the predicted ESR

reached the predefined failure threshold. Accordingly, the predicted RUL at each evaluation time t was calculated as $\hat{RUL}(t) = \hat{T}_f - t$. The actual RUL was calculated as $RUL(t) = T_f - t$, where $T_f$ denotes the actual failure time determined from the measured ESR trajectory. Therefore, the time-wise RUL pairs in Figure 13 were obtained from a single fixed-origin recursive forecast for each channel, rather than from independent forecasts performed at every evaluation time.

To quantitatively evaluate prediction performance, three widely used evaluation metrics were employed: mean absolute error (MAE), root mean square error (RMSE), and mean absolute percentage error (MAPE):

$$MAE = \frac{1}{N}\sum_{i=1}^{N}|\hat{y}_i - y_i| \tag{27}$$

$$RMSE = \sqrt{\frac{1}{N}\sum_{i=1}^{N}(\hat{y}_i - y_i)^2} \tag{28}$$

$$MAPE = \frac{100\%}{N}\sum_{i=1}^{N}\frac{|\hat{y}_i - y_i|}{y_i} \tag{29}$$

Here, $\hat{y}_i$ and $y_i$ denote the predicted and actual RUL, N denotes the total number of valid RUL evaluation samples pooled across the three capacitor channels. The evaluation was performed at the available test sampling instants after each forecast origin of 800, 1000, or 1400 h. The MAE, RMSE, and MAPE were calculated by aggregating the errors over all valid channel–time pairs. The same evaluation samples were used for all three comparison methods to ensure a fair comparison.

The corresponding evaluation results are summarized in Figure 14.

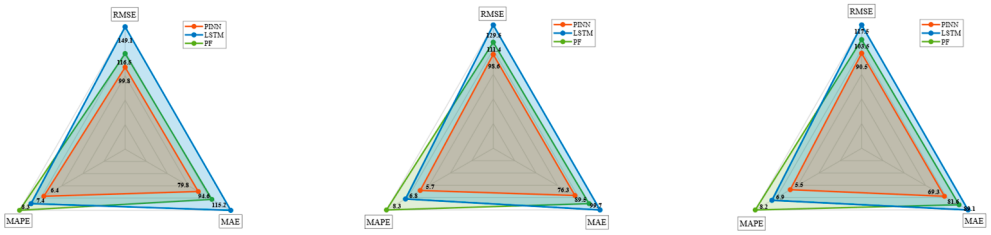
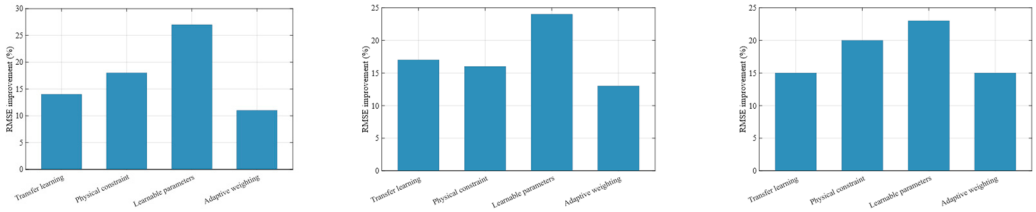



**Figure 14.** Quantitative evaluation of RUL prediction performance: (**a**) 800 h, (**b**) 1000 h, and (**c**) 1400 h.

Across all training-data cutoffs, the proposed PINN achieved the lowest prediction errors among the three methods. When only the first 800 h of degradation data were available, the proposed method achieved an RMSE of 99.8 h, compared with 116.5 h for the LSTM model and 149.1 h for the PF algorithm. These values corresponded to RMSE reductions of 14.3% and 33.1%, respectively. A similar performance advantage was observed in the 1000 h and 1400 h training scenarios. As more degradation data became available, the prediction accuracy of all models improved; however, the proposed PINN maintained a clear performance advantage throughout the prediction horizon.

The superior performance observed in this study could be attributed to three factors. First, the LSTM architecture captured long-term temporal dependencies in the degradation trajectories. Second, the embedded physical degradation model constrained the prediction process and helped prevent physically unrealistic extrapolation. Third, the adaptive optimization mechanism adjusted the physical parameters according to the observed degradation behavior, thereby improving the model's adaptability to varying environmental conditions.

To complement the RUL prediction error comparison presented in the radar chart, an additional ablation study was conducted to investigate the individual contributions of the proposed model components and the sensitivity of physical-parameter learning to initialization. Figure 15 summarizes the RMSE improvement rates associated with transfer learning, physical constraints, learnable physical parameters, and adaptive loss weighting under different training data cutoffs (800, 1000, and 1400 h).




(**a**) (**b**) (**c**)

**Figure 15.** Component-wise RMSE improvement under different target-domain training cutoffs. (**a**) 800 h. (**b**) 1000 h. and (**c**) 1400 h.

Here, a leave-one-component-out strategy was adopted. Specifically, each of the four components (transfer learning, physical constraints, learnable physical parameters, and adaptive loss weighting) was individually removed from the complete PINN, while the other components were kept unchanged. Thus, each bar in Figure 15 represents the RMSE improvement of the complete PINN relative to the corresponding model without one specific component. The detailed configurations of the ablation models are summarized in Table 3.

**Table 3.** Configurations of the ablation experiments.

| Model | Pre-Training | Physical Loss | Physical Parameters ($E_a$, $n$) | Loss Weighting |
|---|---|---|---|---|
| Full PINN | Yes | Included | Learnable | Adaptive |
| w/o Transfer learning | No | Included | Learnable | Adaptive |
| w/o Physical constraint | Yes | Excluded | N/A | N/A |
| w/o Learnable parameters | Yes | Included | Fixed (0.60 eV, 1.50) | Adaptive |
| w/o Adaptive weighting | Yes | Included | Learnable | 0.5 |

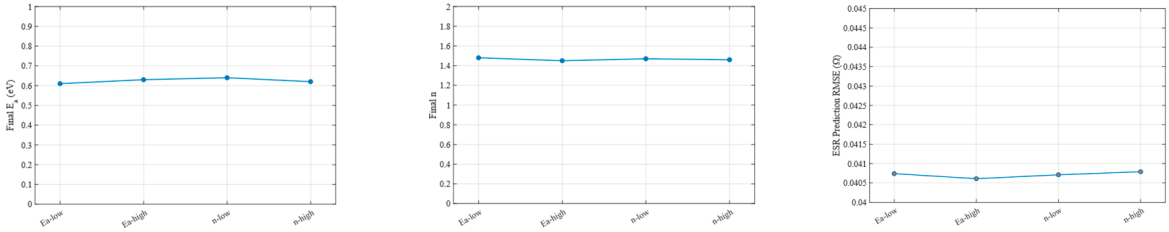
The results revealed differences in the contributions of the four components. The learnable physical-parameter mechanism exhibited the largest RMSE improvement across the three training cutoffs, suggesting that adapting the physical parameters to the observed degradation trajectory improved prediction accuracy. The contribution of the physical constraint became more pronounced as the target-domain training window increased, indicating that a longer observation history could have helped the model exploit degradation-related physical information. Transfer learning also provided positive improvements, although its contribution varied with the training cutoff, reflecting the dependence of transfer effectiveness on the amount of target-domain data available. By comparison, adaptive loss weighting yielded a relatively modest additional reduction in RMSE, suggesting that its primary role was to balance the contributions of the data-driven and physics-based loss terms rather than independently dominate prediction improvement.

While the preceding ablation study in Figure 15 investigated the contributions of individual model components under three target-domain training cutoffs (800, 1000, and 1400 h), an additional initialization sensitivity analysis was conducted to evaluate the influence of physical-parameter initialization on prediction performance. This analysis was performed using the complete PINN configuration under a representative experimental setting, with the target channel and training-data cutoff kept fixed. Specifically, the target

capacitor was the No. 1 channel, and the target-domain training cutoff was 1400 h. The initial values of the activation energy $E_a$, and humidity exponent $n$, were varied independently, while the remaining conditions, including the network architecture and random seed, were kept unchanged. Four initialization combinations were considered, as summarized in Table 4. The final learned physical parameters and the corresponding ESR prediction RMSE were then evaluated, as shown in Figure 16. Unlike Figure 15, this analysis focused specifically on initialization sensitivity rather than component-wise ablation.

**Table 4.** Initial parameter combinations used in the sensitivity analysis.

| Case | Initial Ea (eV) | Initial $n$ |
|---|---|---|
| Ea-low | 0.50 | 1.50 |
| Ea-high | 0.70 | 1.50 |
| n-low | 0.60 | 1.20 |
| n-high | 0.60 | 1.80 |




(**a**) (**b**) (**c**)

**Figure 16.** Sensitivity of physical-parameter learning and ESR prediction to parameter initialization: (**a**) final learned activation energy, (**b**) final learned humidity exponent, and (**c**) ESR prediction RMSE.

Table 4 specifies the low and high initial values used for the activation energy $E_a$ and humidity exponent $n$. These four initialization settings correspond to the four conditions shown on the horizontal axes of Figure 16a–c.

The results showed that the final learned physical parameters and ESR prediction RMSE varied only slightly across the four initialization settings. This indicates that the ESR prediction performance of the proposed PINN was relatively insensitive to the tested initial parameter values under the selected experimental conditions. However, this observation is limited to ESR prediction performance for the investigated target channel and training-data cutoff. It does not establish the robustness of RUL prediction to parameter initialization or the unique identifiability of the physical parameters. In addition, the relatively limited variation in the learned parameters suggests that further investigation under more diverse environmental stress conditions is necessary to better distinguish the individual effects of activation energy and humidity.

Overall, the experimental results demonstrated that the proposed adaptive PINN provided a more accurate, robust, and physically consistent solution for degradation-trajectory prediction and RUL estimation of DC–DC converter capacitors than either purely data-driven or purely physics-based approaches.

To illustrate conditional extrapolation under nominal environmental conditions (25 °C, 50% RH), Figure 17 presents the degradation trajectory predictions of the PINN model trained using data acquired under step-stress conditions.

Figure 17 presents conditional model-based extrapolations of the capacitor degradation trajectories under nominal environmental conditions, using the degradation data collected under step-stress conditions for model development. Under this assumed constant environ-

ment and the specified failure threshold, the predicted times to reach the threshold were 35,856 h, 50,056 h, and 52,072 h, respectively.

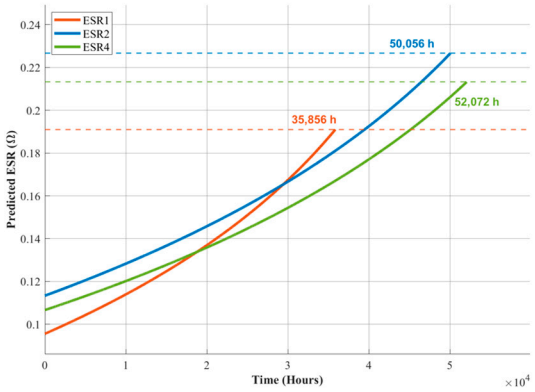



**Figure 17.** Degradation trajectory prediction under nominal operating conditions.

Finally, it should be noted that this study has several limitations. The experimental evaluation is based on three capacitor degradation trajectories obtained from three DC–DC converter channels integrated into a single industrial servo controller. Although these data provide an application-oriented evaluation under step-stress temperature–humidity conditions, the limited number of independent degradation trajectories restricts the statistical generalizability of the results. The repeated measurements collected along each trajectory do not constitute independent component-level replicates. Further validation using additional capacitors and industrial units under diverse operating conditions is therefore necessary to assess the robustness and broader applicability of the proposed framework.

Another limitation of this study is that independent ESR calibration using reference instruments, such as an LCR meter or an impedance analyzer, was not conducted. Therefore, the accuracy of the estimated ESR values could not be independently quantified against reference measurements. The degradation trajectories used for model training and evaluation were obtained using the proposed output voltage ripple-based ESR estimation method. Consequently, the reported prediction performance should be interpreted in the context of these estimated ESR trajectories. Future work will involve independent ESR measurements to further validate the accuracy of the proposed online estimation method.

## 6. Conclusions

This study proposed an adaptive physics-informed neural network (PINN) framework for capacitor remaining useful life (RUL) prediction in DC–DC converters. The proposed framework consisted of two complementary modules with distinct functions.

First, an online equivalent series resistance (ESR) estimation module was developed based on two output voltage ripple samples within a switching period and known circuit parameters. This module enabled ESR to be extracted as a capacitor degradation indicator during normal converter operation without additional excitation signals or system shutdown.

Second, an adaptive LSTM-based PINN prediction module was developed to predict capacitor degradation trajectories and estimate RUL. By incorporating a temperature–humidity-dependent degradation model into the training process, together with learnable physical parameters and adaptive loss weighting, the proposed model combined data-driven temporal learning with physical degradation knowledge. Transfer learning further facilitated adaptation to target capacitors when only limited degradation data were available.

The proposed framework was evaluated using step-stress temperature–humidity accelerated degradation experiments on capacitors embedded in an electro-hydraulic vibration

servo controller. Compared with the LSTM and particle filter (PF) benchmarks, the proposed method reduced the mean percentage error of degradation-trajectory prediction by 44.9% and 38.7%, respectively, and reduced the RUL prediction RMSE by 14.3% and 33.1%, respectively. These results demonstrated the potential of combining online ESR estimation with physics-informed degradation prediction for capacitor health prognostics. Future work will investigate additional coupled electrical, thermal, and mechanical stresses and evaluate the applicability of the framework to other power electronic components.

**Author Contributions:** H.W.: Conceptualization, Investigation, supervision, writing and project administration. X.Z.: Methodology and writing—original draft. J.H.: Data collection and data curation. X.K.: Supervision and data curation. J.P.: Validation and writing—review and editing. All authors have read and agreed to the published version of the manuscript.

**Funding:** This research was funded by the Central Guided Local Science and Technology Development Funded Projects (2025 ZY01081); the National Natural Science Foundation of China under Grant No. 72401261 and the Zhejiang Provincial Natural Science Foundation of China under Grant No. LQN25F030004.

**Data Availability Statement:** The datasets used and analyzed during the current study are available from the corresponding author on reasonable request.

**Acknowledgments:** The authors gratefully acknowledge the research facilities and financial support provided by the Zhejiang Key Laboratory of Reliability Technology for Mechanical & Electrical Product at Zhejiang Sci-Tech University.

**Conflicts of Interest:** The authors declare no conflicts of interest.

## Abbreviations

The following abbreviations are used in this manuscript:

| | |
|---|---|
| RUL | Remaining useful life |
| PINN | Physics-informed neural network |
| ESR | Equivalent series resistance |
| RMSE | Root-mean-square error |
| MAE | Mean absolute error |
| MAPE | Mean absolute percentage error |
| DC | Direct-current |
| MOSFETs | Metal–oxide–semiconductor field-effect transistors |
| AECs | Aluminum electrolytic capacitors |
| MPFCs | Metallized polypropylene film capacitors |
| SVMs | Support vector machines |
| CNN | Convolutional neural network |
| RNNs | Recurrent neural networks |
| LSTM | Long short-term memory |
| CCM | Continuous conduction mode |
| PF | Particle filter |

## References

1. Tarzamni, H.; Babaei, E.; Esmaeelnia, F.P.; Dehghanian, P.; Tohidi, S.; Sharifian, M.B.B. Analysis and Reliability Evaluation of a High Step-Up Soft Switching Push–Pull DC–DC Converter. *IEEE Trans. Reliab.* **2026**, *69*, 1376–1386.
2. Eslamloo, M.K.; Varesi, K.; Tarzamni, H.; Lee, S.S. Comprehensive Reliability Review and Assessment of Switched-Capacitor Step-Up DC–DC Converters. *Reliab. IEEE Trans.* **2025**, *74*, 2766–2778. [CrossRef]
3. K, P.; Vijayakumar, T. Review of Fault Tolerant Power Converters Deployed In Critical Applications. In *Proceedings of the 2021 Second International Conference on Electronics and Sustainable Communication Systems (ICESC)*; IEEE: Piscataway, NJ, USA, 2021; pp. 306–311.
4. Khera, N.; Khan, S.A.; Islam, T.; Agarwala, A.K. An intelligent technique for condition based self-maintenance of aluminum electrolytic capacitors. *Int. J. Syst. Assur. Eng. Manag.* **2016**, *7*, 25–34. [CrossRef]

5. Ahmad, M.W.; Agarwal, N.; Kumar, P.N. Low Frequency Impedance Monitoring and Corresponding Failure Criteria for Aluminum Electrolytic Capacitors. *IEEE Trans. Ind. Electron.* **2017**, *64*, 5657–5666. [CrossRef]
6. Li, H.; Zhang, G.; Wang, Y.; Lin, F. Dependence of Polarization Behaviors on Electrical and Thermal Aging for Pulse Metallized Polypropylene Film Capacitor. *IEEE Trans. Dielectr. Electr. Insul.* **2022**, *29*, 1553–1562. [CrossRef]
7. Pokryvailo, A.; Felicetta, A. Accelerated Aging of HV Metallized Polypropylene Film Capacitors at Sub-kHz Pulsing and Elevated Temperature. *IEEE Trans. Plasma Sci.* **2026**, *54*, 615–622. [CrossRef]
8. Wang, H.; Pei, X.; Wu, Y.; Kang, Y. A General Fault-Tolerant Operation Strategy under Switch Fault for Modular Series-Parallel DC–DC Converter. *IEEE J. Emerg. Sel. Top. Power Electron.* **2020**, *9*, 872–884. [CrossRef]
9. Tang, S.; Wang, J.; Zheng, R.; Wang, D.; Yin, X.; Shuai, Z.; Shen, Z.J. Detection and Identification of Power Switch Failures Using Discrete Fourier Transform for DC-DC Flying Capacitor Buck Converters. *IEEE J. Emerg. Sel. Top. Power Electron.* **2020**, *9*, 4062–4071. [CrossRef]
10. Rojas-Dueñas, G.; Riba, J.-R.; Moreno-Eguilaz, M. Nonlinear Least Squares Optimization for Parametric Identification of DC–DC Converters. *IEEE Trans. Power Electron.* **2021**, *36*, 654–661. [CrossRef]
11. Cen, Z.; Stewart, P. Condition Parameter Estimation for Photovoltaic Buck Converters Based on Adaptive Model Observers. *IEEE Trans. Reliab.* **2017**, *66*, 148–160. [CrossRef]
12. Laadjal, K.; Sahraoui, M.; Cardoso, A.J.M. On-Line Fault Diagnosis of DC-Link Electrolytic Capacitors in Boost Converters, Using the STFT Technique. *IEEE Trans. Power Electron.* **2020**, *36*, 6303–6312. [CrossRef]
13. Liu, Z.; Wang, X.; Chang, G.; Yuan, H.; Tang, W.; Wei, X.; Dai, H. Online Monitoring of Fuel Cell Electrochemical Impedance Spectrum with Multi-stages Multi-sine Signals Based on DC–DC Converter. *IEEE Trans. Power Electron.* **2024**, *39*, 16826–16838. [CrossRef]
14. Miao, J.; Liu, Y.; Yin, Q.; Ju, B.; Zhang, G.; Wang, H. A Novel Soft Fault Detection and Diagnosis Method for a DC/DC Buck Converter Based on Contrastive Learning. *IEEE Trans. Power Electron.* **2024**, *39*, 1501–1513. [CrossRef]
15. Jiang, Y.; Xia, L.; Zhang, J. A Fault Feature Extraction Method for DC–DC Converters Based on Automatic Hyperparameter-Optimized 1-D Convolution and Long Short-Term Memory Neural Networks. *IEEE J. Emerg. Sel. Top. Power Electron.* **2022**, *10*, 4703–4714. [CrossRef]
16. Chen, J.; Miao, J.; Yin, Q. A remaining useful life prediction method of aluminum electrolytic capacitor with adaptive degradation model selection. *Microelectron. Reliab.* **2024**, *162*, 115509. [CrossRef]
17. Jeong, S.H.; Park, J.W.; Kim, H.S. Deep neural network-based lifetime diagnosis algorithm with electrical capacitor accelerated life test. *J. Power Sources* **2024**, *599*, 234182. [CrossRef]
18. Munir, M.; Siddiqui, S.A.; Dengel, A.; Ahmed, S. DeepAnT: A Deep Learning Approach for Unsupervised Anomaly Detection in Time Series. *IEEE Access* **2018**, *7*, 1991–2005. [CrossRef]
19. Soualhi, A.; Makdessi, M.; German, R.; Echeverria, F.R.; Razik, H.; Sari, A.; Venet, P.; Clerc, G. Heath Monitoring of Capacitors and Supercapacitors Using Neo Fuzzy Neural Approach. *IEEE Trans. Ind. Inform.* **2017**, *14*, 24–34. [CrossRef]
20. Li, X.; Zhang, L.; Wang, Z.; Dong, P. Remaining useful life prediction for lithium-ion batteries based on a hybrid model combining the long short-term memory and Elman neural networks. *J. Energy Storage* **2019**, *21*, 510–518. [CrossRef]
21. Li, F.; Li, Q.; Zhang, J.; Kou, J.; Ye, J.; Song, W.; Mantooth, H.A. Detection and Diagnosis of Data Integrity Attacks in Solar Farms Based on Multilayer Long Short-Term Memory Network. *IEEE Trans. Power Electron.* **2021**, *36*, 2495–2498. [CrossRef]
22. Wang, Z.; Qu, J.; Fang, X.; Li, H.; Zhong, T.; Ren, H. Prediction of early stabilization time of electrolytic capacitor based on ARIMA-Bi_LSTM hybrid model. *Neurocomputing* **2020**, *403*, 63–79. [CrossRef]
23. Hong, S.; Feng, T.; Hu, J.; Zhang, X. Operation Security Prediction for Wind Turbines Using Convolutional Neural Networks: A Proposed Method[J/OL]. *IEEE Syst. Man. Cybern. Mag.* **2023**, *9*, 4–9. [CrossRef]
24. Dang, J.; Zheng, H.; Xu, X.; Wang, L.; Hu, Q.; Guo, Y. Adaptive Sparse Memory Networks for Efficient and Robust Video Object Segmentation[J/OL]. *IEEE Trans. Neural Netw. Learn. Syst.* **2025**, *36*, 3820–3833. [CrossRef] [PubMed]
25. Ogliari, E. Deep Learning Regression with Sequences of Different Length: An Application for State of Health Trajectory Prediction and Remaining Useful Life Estimation in Lithium-Ion Batteries. *Batteries* **2024**, *10*, 292. [CrossRef]
26. Hai-Lin, F.; An-Ke, X. A Data Compensation Model for Predicting SOH and RUL of Lithium–Ion Battery. *J. Electr. Eng. Technol.* **2024**, *19*, 395–406. [CrossRef]
27. Meng, Z.; Qian, Q.; Xu, M.; Yu, B.; Yıldız, A.R.; Mirjalili, S. PINN-FORM: A new physics-informed neural network for reliability analysis with partial differential equation. *Comput. Methods Appl. Mech. Eng.* **2023**, *414*, 116172. [CrossRef]
28. Yang, T.; Qian, Z.; Hang, N.; Liu, M. S-PINN: Stabilized physics-informed neural networks for alleviating barriers between multi-level co-optimization. *Comput. Methods Appl. Mech. Eng.* **2010**, *447*, 41.
29. Coulombe, M.A.; Berger, M.; Lesage-Landry, A. Simulation of a closed-loop dc-dc converter using a physics-informed neural network-based model. *Electr. Power Syst. Res.* **2025**, *252*, 112408. [CrossRef]
30. Xiang, Y.; Meng, J.; Du, X.; Lin, H.; Goetz, S.M.; Chung, H.S.-H.; Li, Y.R. Multi-Parameter Estimation of DC-DC Boost Converter via TA-PINN without High-Frequency Measurements. *IEEE Trans. Power Electron.* **2026**, *252*, 112408. [CrossRef]

31. Razmi, P.; Simoes, M.G.; Elmusrati, M. Unified dual-PINN solution for DC-DC power converter modeling and control with fast piecewise CPL sensing. *Electr. Power Syst. Res.* **2026**, *254*, 112671. [CrossRef]
32. Peck, D.S. Comprehensive Model for Humidity Testing Correlation. In *Proceedings of the 24th International Reliability Physics Symposium*; IEEE: Piscataway, NJ, USA, 1986; pp. 44–50.
33. Nakao, H.; Yonezawa, Y.; Nakashima, Y.; Kurokawa, F. *Failure Prediction Using Low Stability Phenomenon of Digitally Controlled SMPS by Electrolytic Capacitor ESR Degradation*; IEEE: Piscataway, NJ, USA, 2017.

**Disclaimer/Publisher's Note:** The statements, opinions and data contained in all publications are solely those of the individual author(s) and contributor(s) and not of MDPI and/or the editor(s). MDPI and/or the editor(s) disclaim responsibility for any injury to people or property resulting from any ideas, methods, instructions or products referred to in the content.